

Magnetic Weyl semimetals with diamond structure realized in spinel compounds

Wei Jiang,¹ Huaqing Huang,² Feng Liu,² Jian-Ping Wang,¹ and Tony Low^{1,*}

¹*Department of Electrical & Computer Engineering,
University of Minnesota, Minneapolis, Minnesota 55455, USA.*

²*Department of Materials Science & Engineering,
University of Utah, Salt Lake City, UT 84112, USA*

(Dated: October 9, 2019)

Diamond-structure materials have been extensively studied for decades, which form the foundation for most semiconductors and their modern day electronic devices. Here, we discover a e_g -orbital ($d_{z^2}, d_{x^2-y^2}$) model within the diamond lattice (e_g -diamond model) that hosts novel topological states. Specifically, the e_g -diamond model yields a 3D nodal cage (3D-NC), which is characterized by a d - d band inversion protected by two types of degenerate states (i.e., e_g -orbital and diamond-sublattice degeneracies). We demonstrate materials realization of this model in the well-known spinel compounds (AB_2X_4), where the tetrahedron-site cations (A) form the diamond sub-lattice. An ideal half metal with one metallic spin channel formed by well-isolated and half-filled e_g -diamond bands, accompanied by a large spin gap (4.36 eV) is discovered in one 4-2 spinel compound (VMg_2O_4), which becomes a magnetic Weyl semimetal when spin-orbit coupling effect is further considered. Our discovery greatly enriches the physics of diamond structure and spinel compounds, opening a door to their application in spintronics.

Known as a new classification of quantum matter¹, quantum topological ordered systems have attracted tremendous attention for exotic physics (e.g., various quantum Hall effect^{2,3}, topological superconductivity⁴, Weyl fermions⁵) and also for promising applications (e.g., spintronics⁶ and quantum computing⁷). In particular, Weyl semimetal materials, characterized with momentum space separated monopole pairs, Fermi arc, and the chiral anomaly, have recently been explored extensively both experimentally and theoretically, as a novel member of the topological family⁸⁻¹⁰. From the inversion-symmetry breaking TaAs family to the time-reversal symmetry breaking magnetic Heusler alloys and Shandite compounds of $M_3M'_2X_2$, a few families of Weyl semimetals have been theoretically proposed and experimentally confirmed¹¹⁻¹⁵. However, most of the studied magnetic Weyl semimetals have either both spin channels entangled near the Fermi level or Weyl points formed far away from the Fermi level^{13,14}, which adds difficulties in studying the intrinsic properties of these Weyl points. It is valuable to search for magnetic Weyl semimetal systems as “clean” as the graphene for Dirac fermions, where the Weyl points is located at the Fermi energy and topological properties can be directly explored and potentially utilized for realistic applications.

The beauty of physics always lie in the simplest models. For example, studies of two-dimensional (2D) graphene have directly spawn various intriguing physical phenomena¹⁶, such as Dirac fermion¹⁷, quantum Spin Hall effect², and superconductivity^{18,19}. It has also stimulated many branches of exciting researches, such as silicene, germanene as its 2D analogues²⁰, valleytronics that utilize k and k' valley degree of freedom^{21,22}, and $p_{x,y}$ -orbital counterpart of graphene with proposed flat band and Wigner crystallization^{23,24}. The diamond structure, which is essentially formed by stacking buckled honeycomb lattice in the A-B-C configuration, can be viewed

as a three-dimensional (3D) analogue of the 2D honeycomb lattice, each containing two atoms in one unit cell. It is therefore the simplest system to study analogous exotic physics in three dimensions. Based on diamond structure, theoretical proposal has indeed been made to achieve topological insulators in three dimensions²⁵, whose proposals has yet been able to be mapped onto real materials. It would be important to identify if there exist such an underlying physical model based on diamond structure that leads to various intriguing topological states and can be realized in real material systems.

One of the most famous family of materials that holds the same group symmetry as diamond structure (Fd-3m) is the spinel compounds (AB_2O_4)²⁶⁻²⁸. With remarkable magnetic properties, spinel compounds has been extensively studied for decades for their promising applications in a broad range, e.g, simple permanent magnets, power handling, and magnetic recording et al²⁹. Surprisingly, its topological properties have been greatly overlooked¹². Careful examination shows that there are several advantages studying the topological properties of spinel compounds: 1) ions located at A sites of the crystal structure form a perfect diamond structure; 2) For most of the transition metal ions in A sites, the localized d orbitals are widely separated from other orbitals, which could yield ideal band structure with clean topological features; 3) The versatility and high tunability of spinel compounds provide a wide range of material candidates with either magnetic or nonmagnetic options; 4) Mature synthesize technology will facilitate its future application in real devices.

Here, based on tight-binding analysis, we develop a novel two e_g -orbitals (d_{z^2} and $d_{x^2-y^2}$) model on the diamond structure (e_g -diamond model), as a 3D analogue of the 2D $p_{x,y}$ -graphene model²³. When both nearest-neighbor (NN) and next-NN (NNN) interaction are considered, the e_g -diamond bands form a Dirac/Weyl

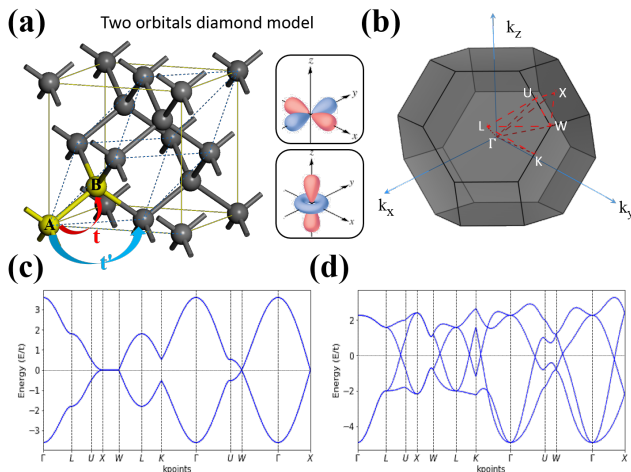


FIG. 1. Topological semimetal in e_g -orbital diamond model. **a** Two-orbital diamond model with nearest-neighbor t and next nearest neighbor hopping t' . Insets show the d_{z^2} and $d_{x^2-y^2}$ orbitals for the given coordinates. **b** First-Brillouin zone with high-symmetry k-points and k-paths. **c** Band structure of double degenerate single-orbital diamond model with only the NN hopping along high-symmetry paths shown in **b**. **d** Band structure of e_g -diamond model with nonzero NNN hopping t' , showing various linear crossing around the Fermi level.

nodal cage (NC) in the 3D Brillouin zone with hourglass fermions corresponding to the Dirac/Weyl points in the 2D case. The hourglass fermions involved are protected by the coexistence of e_g orbitals degeneracy and diamond crystal symmetry with A, B sublattices degeneracy. Furthermore, we demonstrate a real material realization of the model in a representative 4-2 spinel compounds ($V^{4+}Mg_2^{2+}O_4$) using first-principles calculations. The spin-polarized e_g -diamond bands are exactly half-filled and isolated from other bands because of the strong tetrahedron crystal field splitting and the exchange splitting. The spin-orbit coupling effect further breaks the degeneracy of the 3D-NC, leading to the magnetic Weyl semimetal state. It is exciting to note that VMg_2O_4 has excellent lattice matching (and chemical compatibility) with MgO , which is a widely used spintronics oxide material in industry. This opens the door for the realization of novel spintronics devices, such as achieving low switching energy magnetic devices.

TIGHT BINDING MODEL

Different from the well-known sp^3 or sp^3s^* diamond model, we present here a 3D e_g -diamond model. For a diamond structure (space group Fd-3m) with the face-centered cubic (FCC) Bravais lattice, there are two equivalent atomic sites in each unit cell (blue dashed line), labelled as A and B, as shown in Fig.1a. By choosing the coordinates in Fig.1a as the orbital quantization axes, we

select two energetically degenerate atomic $d_{x^2-y^2}$ and d_{z^2} orbitals (e_g orbitals due to local tetrahedral crystal field splitting) on each site for the e_g -diamond model. Without including the spin degree of freedom, this e_g -diamond model can be essentially described by a four-band Hamiltonian. It can be viewed as a 3D extension of the 2D p_x, p_y -graphene four-band model, in which each honeycomb site is occupied by atomic p_x and p_y orbitals²³. To succinctly demonstrate the physics, we limit our Hamiltonian to only the essential NN (t) and NNN (t') interactions, and the Hamiltonian can be written as:

$$\mathcal{H} = \sum_i \epsilon_i d_i^\dagger d_i + \sum_{\langle i,j \rangle} t_d d_i^\dagger d_j + \sum_{\langle\langle i,j \rangle\rangle} t'_{ij} d_i^\dagger d_j + H.c., \quad (1)$$

where ϵ_i represents the on-site energy of state at i site; d_i^\dagger and d_i are the creation and annihilation operators of d electrons at the site i , respectively; t_d and t'_{ij} are the NN and NNN hoppings, respectively. In the diamond structure, each atom has four NNs and twelve NNNs. Given the strict orthogonality between the two e_g orbitals, the NN hopping term between d_{z^2} and $d_{x^2-y^2}$ is set as zero. The non-zero NN hopping terms are among d_{z^2} or $d_{x^2-y^2}$ orbitals, which have the same hopping amplitude t_d for different e_g orbitals and also along different directions along four tetrahedron directions. More extensive TB-model with parameters based on Slater-Koster matrix also confirms these features (Supplementary note 1).

In the absence of the NNN interactions, the same amplitude between hoppings among d_{z^2} orbitals and that among $d_{x^2-y^2}$ orbitals guarantees the double degeneracy of the bands. This can be understood as two exact copies of single-orbital diamond model due to the degeneracy of two e_g orbitals on each site, as can be seen from the band structure shown in Fig.1c (Supplementary note 1). On the other hand, in the single-orbital diamond model, the same hopping amplitude along different directions enables the formation of Dirac nodal lines along X-W path because of the six 2-fold rotation symmetries (C_2 axis along x, y, and z directions through A and B sites) in the point group $m3m$ (O_h). Therefore, as shown in Fig.1c, the NN e_g -diamond model produces a double degenerate two band structure with 4-fold degenerate lines along X-W k-path. It is straightforward that X-W and its inversion and rotational symmetric paths (four 3-fold rotation axis along tetrahedral bond direction) will have the same degeneracy. It is important to emphasize that there exist two types of band degeneracies: one type is due to the degeneracy of e_g orbitals (named type-A thereafter, d_{z^2} and $d_{x^2-y^2}$) and the other type owing to the C_2 rotational symmetry in the single-orbital diamond Hamiltonian (named type-B thereafter, d_{z^2} or $d_{x^2-y^2}$ in A and B sites).

Next, we include the NNN hopping interactions, where NNNs form the FCC structure. There are two types of NNN hoppings, i.e., hoppings between d_{z^2} and $d_{x^2-y^2}$ orbitals (termed type-I thereafter, t_1), and hoppings among $d_{z^2}/d_{x^2-y^2}$ orbitals (termed type-II thereafter, t_2). Con-

sidering each single-orbital diamond Hamiltonian as one block, the type-I hopping terms mix the two unit blocks by introducing the off-diagonal interaction, and the type-II hopping terms act as on-site energy variation of the two blocks (Supplementary note 1). Let us examine effects of these two types of NNN interactions to the band structure. First, it is apparent that if t_2 remains the same for e_g orbitals, i.e., same variation of the on-site energies, the band degeneracy remains, leading to a similar band structure with slightly different dispersion (Supplementary Fig. 2). Only different t_2 can lift the type-A degeneracy of those two bands. On the other hand, any non-zero t_1 will lift the type-A degeneracy due to the off-diagonal orbital mixing.

Interestingly, we notice that under some symmetric hopping conditions, the band degeneracy along certain high-symmetry k-paths remains even for nonzero t_1 and different t_2 NNN hoppings. Specifically, we find that at the center point of the eight hexagonal Brillouin boundary (K_{HC}), the type-A degeneracy remains when the NNN hopping Hamiltonian keeps the C_4 rotational symmetry. Similarly, at the Γ and any point between Γ and K_{HC} , the band degeneracy will remain while both C_4 rotational symmetry and the summation of hoppings along 12 NNN (3 nonequivalent) directions equals to zero (Supplementary note 1 and Supplementary Fig. 3). Note the type-B degeneracy along X-W path is also conserved as the C_2 rotation symmetry remains. One important outcome of the coexistence of two types of band degeneracy is the guaranteed band crossing (nodal point, hourglass fermion) along certain k-paths, when the two terminal k-points have different types of degeneracies, as shown in Fig. 1b. Such band crossing can be understood from the continuity nature of the wavefunctions that essentially leads to a $d-d$ band inversion, since the two degenerate bands are formed with different orbital states (Supplementary Fig. 3). As a consequence, those nodal points surprisingly construct a three-dimensional nodal cage, which will be further discussed later.

MAGNETIC SEMIMETAL IN SPINEL COMPOUNDS

To realize the aforementioned e_g -diamond model in real materials, we focus our attention on the well known spinel compounds that also have a space group of Fd-3m as that of the diamond structure²⁶⁻²⁸. These inorganic oxides, with a chemical formula of AB_2O_4 , are constructed by FCC lattice of O^{2-} anions and interstitial cations in tetrahedral (T-site) and octahedral (O-site) sites formed by O^{2-} ions, as shown in Fig.2a. Sulphur or other chalcogenides could also be used as anions, and the corresponding compounds are normally termed as thiospinel. There are eight tetrahedral and four octahedral sites in the spinel compounds. In a normal spinel structure, cations A occupy one-eighth of the T-sites and cations B occupy one-half of the O-sites. There are also

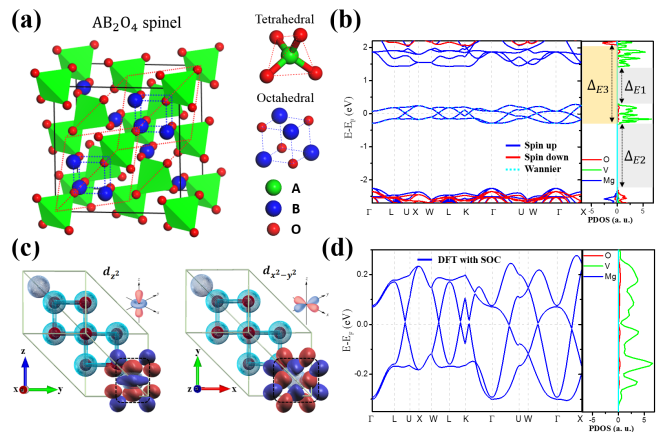


FIG. 2. **Electronic and magnetic properties of VMg_2O_4 .** **a** Conventional atomic structure of an ionic spinel compound with chemical formula of AB_2O_4 with the primitive unit cell labelled using dashed red lines. Cations A and B occupy the tetrahedral and octahedral sites, respectively. **b** Band structure of 4-2 spinel ($V^{4+}Mg_2^{2+}O_4$), showing half-filled four-band structure isolated from the other bands with $d-d$ crystal splitting gap Δ_{E1} , $p-d$ charge transfer gap Δ_{E2} , and exchange splitting gap Δ_{E3} . **c** Maximally localized wannier functions of d_{z^2} and $d_{x^2-y^2}$ orbitals from wannier fitting. **d** Enlarged four-band structure near the Fermi level from DFT and the wannier fitting, respectively.

inverse spinel and mixed spinel structures that have A and B ions filling different O- and T- sites. Here, we will only focus on the normal spinel compounds with each types of polyhedron site occupied by the same type of metal cations. These normal spinels can be further classified into two categories based on the valence states of the cations, i.e., 2-3 spinel with A^{2+} and B^{3+} ; 4-2 spinel with A^{4+} and B^{2+} . It is important to mention that the A cations in T-sites form exactly a diamond structure and B cations in O-sites form a 3D kagome lattice instead. The 3D kagome lattice has been well-documented in other oxide compounds, such as pyrochlore (Fd-3m) with the chemical formula of $A_2B_2O_7$ ³⁰, which was predicted to hold magnetic Weyl semimetal state and 3D flat band^{11,31,32}. However, to the best of our knowledge, though the diamond structure made by transition metal ions exist in many compounds, their intriguing electronic and topological properties have not been studied.

For A cations, the local tetrahedral crystal field splits the five degenerate d orbitals into three-fold degenerate t_{2g} and two-fold degenerate e_g orbitals with relatively lower energies. Further exchange splitting of these d -orbitals will break the time reversal symmetry and lift the spin degeneracy (Supplementary note 2 and Supplementary Fig. 4). With proper filling of the e_g orbitals, e.g., one electron per site, it could form a half-filled magnetic e_g -diamond bands around the Fermi level. Indeed, we found one experimentally studied 4-2 spinel compound with chemical formula of VMg_2O_4 that perfectly satisfies these criteria^{33,34}, where vanadium cations ($4s^23d^3$) have

one d electron left after donating four valence electrons (V^{4+}) to neighboring oxygen anions (O^{2-}). Therefore, we carried out first-principles calculation (see methods) to study its electronic and magnetic properties. The calculations show that VMg_2O_4 is a ferromagnetic (FM) material with a magnetic moment of $2 \mu_B$ per unit cell (UC), which are mainly contributed by the V cations, as confirmed by the spin distribution plot (Supplementary Fig. 5). The energy difference between FM and antiferromagnetic (AFM) state is around 0.43 eV at the PBE level, indicating a promising room temperature FM feature (Supplementary note 3 and Supplementary Fig. 5).

We first calculated the band structure of VMg_2O_4 without considering the spin-orbit coupling (SOC) effect. As shown in Fig.2b, there is a clear four-band structure right at the Fermi level with very good isolation from other bands. The band structure exhibits an ideal half-metallicity feature where one spin channel is metallic and the other spin channel is insulating with a band gap as large as 4.36 eV at the PBE level of accuracy. We further calculated the system using hybrid functionals, which shows the same feature with a even larger spin gap (5.17 eV for meta-GGA and 6.62 eV for HSE, Supplementary Fig. 6). As we are interested in the four-band structure, we will use the PBE results for simplicity. To understand this peculiar electronic structure, we plotted and analyzed the projected density of states (PDOS) of VMg_2O_4 . As shown in Fig.2b, the four bands around the Fermi level are nearly half-filled and mainly contributed by V d electrons, which is consistent with the magnetic moment distribution. The PDOS of Mg ions are found located far above the Fermi level, as the two valence electrons are fully transferred to O^{2-} ions to form the Mg^{2+} with zero valence electrons. The oxygen state are about 2 eV below the Fermi level because of the closed shell electronic configuration after gaining electron from Mg and V.

The observed band isolation in spin up channel can be traced to the underlying energy splittings indicated as Δ_{E1} and Δ_{E2} , as shown in Fig.2b. The energy gap above (Δ_{E1}) is between d orbitals, which essentially is the tetrahedral crystal field splitting energy (Δ_{tet}) between e_g and t_{2g} orbitals. The large separation, $\Delta_{tet} \approx 2$ eV, is due to the strong interaction with O^{2-} ions and the high oxidation state of V^{4+} . The energy gap below the Fermi level (Δ_{E2}) is between d and p orbitals, which is the charge-transfer gap determined basically by the energy-level separation of orbitals between vanadium and oxygen ligand. The separation can be well characterized by the ligand electronegativity and the Madelung potential³⁵. On the other hand, the large band gap in the spin down channel can be understood as the cooperative effect of Δ_{E2} and large Δ_{E3} . Δ_{E3} is essentially the exchange splitting of the V d electrons, which is known to be significant because of the strong localization effect of transition metal d orbitals. Ideally, such large gap would guarantee pure spin current and prevent any current leakage of the

minority spin. To the best of our knowledge, this is also the largest spin gap among reported half-metallic ionic compounds.

E_g -DIAMOND MODEL AND 3D-NC IN VMg_2O_4

More interestingly, a closer look at these four bands (Fig.2b) reveals multiple linear crossings around the Fermi level, indicating a semimetallic feature. This is also supported by the enlarged PDOS plot, which shows nearly zero DOS around the Fermi level (Fig.2d). Besides those crossings (nodal points), there also exist several degenerate bands along Γ -L, X-W. These features agree perfectly with our e_g -diamond model, and the slight difference of band dispersion is simply due to the different hopping integrals, which will not affect the crossing features of interest. To confirm the e_g -diamond model, we performed the maximally localized Wannier functions (MLWFs) calculation to fit to the DFT band structures using the Wannier90 package³⁶. The MLWFs fitted band structure based on two e_g -orbitals on diamond lattice agrees perfectly with the DFT result, as can be seen in Fig.2b. Furthermore, the calculated MLWFs show clearly the shape of d_{z^2} and $d_{x^2-y^2}$, as shown in Fig.2c, confirming the orbital characteristics and again validating the e_g -diamond model. This is further supported from the band-resolved partial charge distribution plot of these four bands, which show a characteristic shape composed of the two orbitals (Supplementary Fig. 7).

As demonstrated from the e_g -diamond model, we expect the band structure of VMg_2O_4 will also form a nodal cage in the 3D first-Brillouin zone. To confirm the 3D nodal cage feature, we first calculated 3D band structures in two 2D k -planes with one plane at the hexagonal Brillouin boundary [(111) surface] and the other one at k_x - k_y plane across the Γ point [(110) surface], as shown in Fig.3a and c, respectively. The 3D band structure (Supplementary Fig. 8) and the band gap between the middle two Dirac bands (Fig.3b and d) show clearly nodal ring features within both the hexagon (111) and octagon (110) plane, respectively. According to the C_4 rotational symmetry and the inversion symmetry, the other seven hexagonal Brillouin zone boundaries also possess the same feature as (111) surface (Supplementary Fig. 8). Similarly, symmetry invariant planes, i.e., (101) and (011) planes across the Γ point, of (110) surface possess the same feature due to the C_3 rotational symmetry (Supplementary Fig. 8).

From the band structure in Fig.2b, we can see nearly all the nodal points are located closely adjacent to the Fermi level (< 20 meV). Therefore, the Fermi surface could essentially capture the 3D nodal cage feature. Indeed, the Fermi surface plot, as shown in Fig.3e, shows a smooth 3D surface within the 3D Brillouin zone that ends at the hexagonal Brillouin zone boundaries, which interestingly has a similar shape as seen in Cu metal³⁷. Because of the small energy dispersion of the nodal cage,

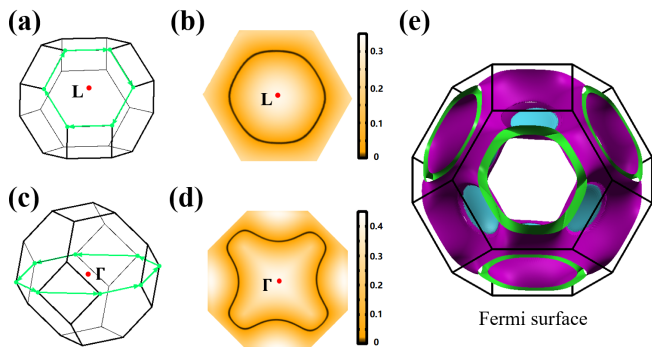


FIG. 3. **3D Nodal cage.** **a** 2D hexagonal k-plane of the (111) surface at the Brillouin zone edge. **b** Band gap between the middle two bands for the 2D k-plane in **a**. **c** and **d** same as **a** and **b** for the 2D octagonal k-plane of the (110) surface across the Γ point of the 3D Brillouin zone. **e** Fermi surface at the energy of Fermi level, showing the feature of 3D nodal cage. Purple and blue regions represent the hole and electron pockets, respectively. Green region highlights the cross section at the Brillouin zone boundary.

we see the coexistence of electron and hole pockets, where hole pockets are mostly located near the square zone boundaries. The cross sections of the 3D Fermi/nodal cage for different planes (2D Fermi surface, Supplementary Fig. 9 and 10) are also consistent with previously demonstrated nodal rings feature based on 3D band structure calculations. It is found that the nodal line within (111) surface is nearly flat, while that of (110) surface shows clear energy oscillation (± 20 meV) as it cut across the square zone boundaries. We also calculated the 3D band structure and 2D Fermi surface for two series of 2D k-planes (Supplementary Fig. 9-11), i.e., (111) planes and (110) planes from the boundary to the center of the Brillouin zone with a step of 0.1 \AA , which further confirm the intriguing 3D nodal cage feature.

MAGNETIC WEYL SEMIMETAL

Generally, such nodal cage is not robust, which will become gapped after considering SOC effect^{38,39}. Depending on whether the system becomes fully gapped or not, the material will become the quantum anomalous Hall insulator or magnetic Weyl semimetal. Therefore, we proceed to include the SOC to determine the topological phases of the spinel compound VMg_2O_4 . Firstly, we performed the non-collinear calculations with different spin configurations (Supplementary note 4), which show that the system continues to be FM with nearly degenerate energies along different magnetization directions. The corresponding band structure for the magnetization direction along $\langle 111 \rangle$ direction is plotted along high-symmetry k-paths (Fig.2d), where most of the nodal points become gapped with several k-points remaining degenerate, such as that along Γ -W that is perpendicular to the magnetic field. This is a known effect in

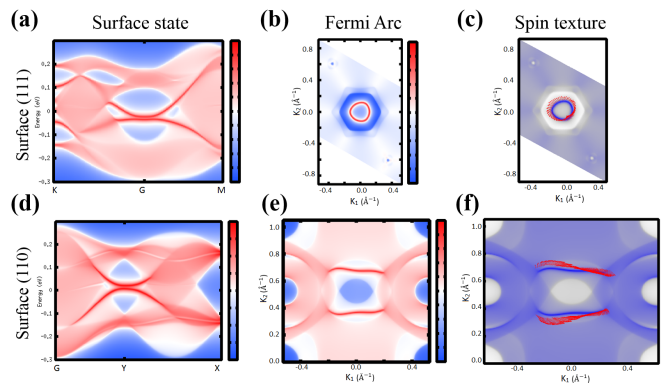


FIG. 4. **Topological properties of Weyl semimetal VMg_2O_4 .** **a** Topological surface state connecting bulk states for the (111) surface. **b** and **c** Fermi arc and the corresponding spin texture of the (111) surface. **d**, **e**, and **f** Same as **a**, **b**, and **c** for (110) surface.

magnetic Weyl semimetal system, where the positions of Weyl points are dependent on the magnetization direction³². Further detailed calculations show that there exist 18 pairs of degenerate points within the first Brillouin zone, which are confirmed to be Weyl pairs with Berry phase of $\pm\pi$ through the Berry curvature integration around these points (Supplementary Fig. 12 and Supplementary Table 1).

To demonstrate the topological properties of this magnetic Weyl semimetal, we first calculated the surface state using a semi-infinite system based on Green's function. As can be seen from Fig.4a and d, topological non-trivial surface states connecting the bulk states can be clearly seen for both (111) and (110) surfaces, respectively. As one of the characteristic feature of the Weyl semimetals, the Fermi arc for these two surfaces are also calculated, as shown in Fig.4b and e. The Fermi arcs show dramatic difference between different surfaces due to different projection of Weyl pairs. For the (110) surface, two pairs of Weyl points can be clearly seen from the two separated Fermi arcs as required by the C_2 rotational symmetry. For the (111) surface, the Fermi arcs form a "Fermi ring" with three pairs of Weyl points due to the C_3 rotational symmetry. These Weyl points are accidentally overlapping while projecting to the (111) surface, which are essentially separated within the bulk Brillouin zone. The spin textures of the Fermi arc shown in Fig.4c and f indicate the positive and negative chirality of Weyl points, which are further confirmed from the Berry phase calculation by integrating the Berry curvature along the surface enclosing the Weyl points.

DISCUSSION AND PERSPECTIVES

One of the intriguing properties of Weyl semimetal is their proposed large intrinsic anomalous Hall conductivity σ_H^A , which comes from the integration of Berry

curvature of bulk band structure with Weyl points^{40,41}. Considering the small charge current σ due to the semi-metallic feature, it is believed that Weyl semimetal could yield a large anomalous Hall angle σ_H^A/σ . Therefore, we also calculated intrinsic anomalous Hall conductivity of VMg_2O_4 , which shows a relatively large peak ($\approx 100 \Omega^{-1} \cdot \text{cm}^{-1}$) around the Fermi level (Supplementary Fig. 13). We note that σ_H^A of VMg_2O_4 is much smaller than the largest σ_H^A reported in literature^{15,42}. This is reasonable as in VMg_2O_4 , only those nodal points contribute to the σ_H^A around the Fermi level. Though the Weyl points may serve as hot spot with extremely large Berry curvature, the contribution from positive and negative Weyl points may cancel each other and lead to a relatively small total σ_H^A . Theoretical proposals suggest engineering extra bulk bands to cross the Fermi level, which may help contributing to large σ_H^A ⁴³, though the system is no longer a Weyl semimetal. To test this idea, we modified the band dispersion through strain engineering and successfully realize the proposed band structure upon compressive strain. We further calculate the σ_H^A , which indeed show a large enhancement of the σ_H^A by at least 2-folds (Supplementary Fig. 13).

The intriguing phenomenon observed in VMg_2O_4 can also be extended to other spinel compounds. Through theoretical calculations, we find the spinel compounds formed with elements having the same valence states as VMg_2O_4 , e.g., VMg_2Se_4 and VCa_2O_4 , share the same features as VMg_2O_4 , i.e., magnetic Weyl semimetal phase with e_g -diamond model (Supplementary Fig. 14). On the other hand, based on the same model, with different electron filling, some other potentially interesting phases can be realized with elements having different valence states. For example, we can acquire large gap (≈ 3 eV) half-metal phase in MnMg_2O_4 and realize an FM insulating state in CrMg_2O_4 (Supplementary Fig. 14). It is interesting to mention that FM insulator possesses two different band gaps (0.6 eV and 3.6 eV) in different spin channels, which could potentially be used as spin filter in magnetic tunneling junction devices.

On the other hand, the lattice compatibility/match with (001) textured MgO tunneling barrier is critical for practical applications. Many materials, such as heusler materials, that have been proposed and/or studied faces practical integration issues with MgO because of lattice mismatch. Interestingly, the material we studied here has a very small lattice mismatch with MgO for both

(001) and (111) planes ($< 0.4\%$), because of their structural similarity (Supplementary Fig. 15). This lattice matching might facilitate high quality growth of VMg_2O_4 directly on top of MgO to study or utilize its intriguing magnetic Weyl semimetal features, as good quality MgO thin films have been easily grown and widely utilized for spintronic devices. For example, we can build MTJ devices with $\text{VMg}_2\text{O}_4/\text{MgO}/\text{VMg}_2\text{O}_4$ stacking or simply use VMg_2O_4 as the spin filtering layer (Supplementary Fig. 16). We note that there also exist a well-studied 2-3 vanadium spinel, MgV_2O_4 , which contains the same types of elements but different stoichiometric ratio, valence states, as well as occupation of cations^{44,45}. MgV_2O_4 is found to be a spin-1 AFM insulator with strong frustration due to the 3D kagome lattice formed by the magnetic V ions, which is dramatically different from that of VMg_2O_4 discussed here. In order to get the VMg_2O_4 phase with high valence state V^{4+} experimentally, relatively high oxygen pressure and Mg:O ratio might be necessary^{33,34}.

CONCLUSION

In summary, we have discovered a novel e_g -diamond four-band model which yields intriguing nodal cage feature due to the coexistence of orbital and sublattice degeneracies. We discovered that such model can be realized in the well-studied spinel oxide compounds. Using 4-2 spinel compound VMg_2O_4 as a representative example, we confirmed the validity of the e_g -diamond model and demonstrate the formation of 3D nodal cage due to linear crossing between the middle two bands. Its topological properties are studied, indicating the material to be a magnetic Weyl semimetal, which is novel to the spinel compounds. We further expand the model to a series of spinel compounds and demonstrate their promising applications as spintronic materials. This theoretical discovery substantially enriches the physics of spinel compounds and could potentially lead to new applications.

Acknowledgement. This project is supported by SMART, one of seven centers of nCORE, a Semiconductor Research Corporation program, sponsored by National Institute of Standards and Technology (NIST). We thank the MSI at the University of Minnesota for providing the computing resources.

* Corresponding author: tlow@umn.edu

¹ X.-G. Wen, Rev. Mod. Phys. **89**, 041004 (2017).

² C. L. Kane and E. J. Mele, Phys. Rev. Lett. **95**, 226801 (2005).

³ M. Z. Hasan and C. L. Kane, Rev. Mod. Phys. **82**, 3045 (2010).

⁴ X.-L. Qi and S.-C. Zhang, Rev. Mod. Phys. **83**, 1057 (2011).

⁵ B. Yan and C. Felser, Annual Review of Condensed Matter Physics **8**, 337 (2017).

⁶ D. Pesin and A. H. MacDonald, Nature Materials **11**, 409 (2012).

⁷ J. Moore, Nature Physics **5**, 378 (2009).

⁸ A. A. Burkov and L. Balents, Phys. Rev. Lett. **107**, 127205 (2011).

⁹ B. Q. Lv, H. M. Weng, B. B. Fu, X. P. Wang, H. Miao,

- J. Ma, P. Richard, X. C. Huang, L. X. Zhao, G. F. Chen, Z. Fang, X. Dai, T. Qian, and H. Ding, *Phys. Rev. X* **5**, 031013 (2015).
- ¹⁰ C. Shekhar, A. K. Nayak, Y. Sun, M. Schmidt, M. Nicklas, I. Leermakers, U. Zeitler, Y. Skourski, J. Wosnitza, Z. Liu, Y. Chen, W. Schnelle, H. Borrmann, Y. Grin, C. Felser, and B. Yan, *Nature Physics* **11**, 645 (2015).
- ¹¹ X. Wan, A. M. Turner, A. Vishwanath, and S. Y. Savrasov, *Phys. Rev. B* **83**, 205101 (2011).
- ¹² G. Xu, H. Weng, Z. Wang, X. Dai, and Z. Fang, *Phys. Rev. Lett.* **107**, 186806 (2011).
- ¹³ C. Felser, L. Wollmann, S. Chadov, G. H. Fecher, and S. S. P. Parkin, *APL Materials* **3**, 041518 (2015).
- ¹⁴ Z. Wang, M. G. Vergniory, S. Kushwaha, M. Hirschberger, E. V. Chulkov, A. Ernst, N. P. Ong, R. J. Cava, and B. A. Bernevig, *Phys. Rev. Lett.* **117**, 236401 (2016).
- ¹⁵ E. Liu, Y. Sun, N. Kumar, L. Muechler, A. Sun, L. Jiao, S.-Y. Yang, D. Liu, A. Liang, Q. Xu, J. Kroder, V. S. H. Borrmann, C. Shekhar, Z. Wang, C. Xi, W. Wang, W. Schnelle, S. Wirth, Y. Chen, S. T. B. Goennenwein, and C. Felser, *Nature Physics* **14**, 1125 (2018).
- ¹⁶ A. H. Castro Neto, F. Guinea, N. M. R. Peres, K. S. Novoselov, and A. K. Geim, *Rev. Mod. Phys.* **81**, 109 (2009).
- ¹⁷ K. S. Novoselov, A. K. Geim, S. V. Morozov, D. Jiang, M. I. Katsnelson, I. V. Grigorieva, S. V. Dubonos, and A. A. Firsov, *Nature* **438**, 197 (2005).
- ¹⁸ B. Uchoa and A. H. Castro Neto, *Phys. Rev. Lett.* **98**, 146801 (2007).
- ¹⁹ Y. Cao, V. Fatemi, S. Fang, K. Watanabe, T. Taniguchi, E. Kaxiras, and P. Jarillo-Herrero, *Nature* **556**, 43 (2018).
- ²⁰ P. Vogt, P. De Padova, C. Quaresima, J. Avila, E. Frantzeskakis, M. C. Asensio, A. Resta, B. Ealet, and G. Le Lay, *Phys. Rev. Lett.* **108**, 155501 (2012).
- ²¹ D. Gunlycke and C. T. White, *Phys. Rev. Lett.* **106**, 136806 (2011).
- ²² Y. Jiang, T. Low, K. Chang, M. I. Katsnelson, and F. Guinea, *Phys. Rev. Lett.* **110**, 046601 (2013).
- ²³ C. Wu, D. Bergman, L. Balents, and S. Das Sarma, *Phys. Rev. Lett.* **99**, 070401 (2007).
- ²⁴ W. Jiang, Z. Liu, J.-W. Mei, B. Cui, and F. Liu, *Nanoscale* **11**, 955 (2019).
- ²⁵ L. Fu, C. L. Kane, and E. J. Mele, *Phys. Rev. Lett.* **98**, 106803 (2007).
- ²⁶ D. S. McClure, *Journal of Physics and Chemistry of Solids* **3**, 311 (1957).
- ²⁷ P. K. Baltzer, H. W. Lehmann, and M. Robbins, *Phys. Rev. Lett.* **15**, 493 (1965).
- ²⁸ K. E. Sickafus, J. M. Wills, and N. W. Grimes, *JACS* **82**, 3279.
- ²⁹ R. Valenzuela, *Phys. Research International* **2012** (2012), 10.1155/2012/591839.
- ³⁰ J. S. Gardner, M. J. P. Gingras, and J. E. Greedan, *Rev. Mod. Phys.* **82**, 53 (2010).
- ³¹ W. Witczak-Krempa and Y. B. Kim, *Phys. Rev. B* **85**, 045124 (2012).
- ³² Y. Zhou, K.-H. Jin, H. Huang, Z. Wang, and F. Liu, *Phys. Rev. B* **99**, 201105 (2019).
- ³³ H. Oshima, S. Shirasaki, and H. Yamamura, *JACS* **60**, 277 (1977).
- ³⁴ J. R. Hellmann and V. S. Stubican, *JACS* **66**, 265 (1983).
- ³⁵ Y. Ohta, T. Tohyama, and S. Maekawa, *Phys. Rev. Lett.* **66**, 1228 (1991).
- ³⁶ N. Marzari and D. Vanderbilt, *Phys. Rev. B* **56**, 12847 (1997).
- ³⁷ B. Segall, *Phys. Rev.* **125**, 109 (1962).
- ³⁸ H. Huang, W. Jiang, K.-H. Jin, and F. Liu, *Phys. Rev. B* **98**, 045131 (2018).
- ³⁹ H. Chen, S. Zhang, W. Jiang, C. Zhang, H. Guo, Z. Liu, Z. Wang, F. Liu, and X. Niu, *J. Mater. Chem. A* **6**, 11252 (2018).
- ⁴⁰ C. Zeng, Y. Yao, Q. Niu, and H. H. Weitering, *Phys. Rev. Lett.* **96**, 037204 (2006).
- ⁴¹ S. Onoda, N. Sugimoto, and N. Nagaosa, *Phys. Rev. Lett.* **97**, 126602 (2006).
- ⁴² Q. Wang, Y. Xu, R. Lou, Z. Liu, M. Li, Y. Huang, D. Shen, H. Weng, S. Wang, and H. Lei, *Nature Communications* **9**, 3681 (2018).
- ⁴³ E. Derunova, Y. Sun, C. Felser, S. S. P. Parkin, B. Yan, and M. N. Ali, *Science Advances* **5** (2019), 10.1126/sciadv.aav8575.
- ⁴⁴ O. Tchernyshyov, *Phys. Rev. Lett.* **93**, 157206 (2004).
- ⁴⁵ S.-H. Lee, D. Louca, H. Ueda, S. Park, T. J. Sato, M. Isobe, Y. Ueda, S. Rosenkranz, P. Zschack, J. Íñiguez, Y. Qiu, and R. Osborn, *Phys. Rev. Lett.* **93**, 156407 (2004).